Understanding of Oxygen Reduction Reaction by examining carbon-oxygen gasification reaction and carbon active sites on metal and heteroatoms free carbon materials of different porosities and structures

*Atsushi Gabe[a], Ramiro Ruiz-Rosas[a], Emilia Morallón[b], Diego Cazorla-Amorós[a]**

a Instituto Universitario de Materiales, Departamento de Química Inorgánica, Universidad de Alicante, Apartado 99, 03080-Alicante, Spain

b Instituto Universitario de Materiales, Departamento de Química Física, Universidad de Alicante, Apartado 99, 03080-Alicante, Spain

*Corresponding author. Tel: (+34) 96 590 3400. E-mail: cazorla@ua.es (D.C.A.)

Abstract

Knowledge of the carbon active sites for Oxygen Reduction Reaction (ORR) remains confusing and controversial and thus the detailed mechanism is still not clarified. Considering the nature of the carbon-oxygen interaction in active sites during the gasification reaction, it could be inferred that the sites for this reaction are the same as those participating in the ORR. Herein, the relationship between carbon-oxygen gasification properties and ORR activities was elucidated. Carbon materials including different structures and porosities were selected and extensively characterized in terms of structural and electrochemical properties. Regarding gasification properties, active surface area (ASA) and reactivity for carbon-oxygen reaction were determined. A good linear correlation is found between ORR activity and carbon-oxygen gasification reactivity. Interestingly, similar correlation is found between ORR activity or gasification reactivity and ASA, although two different slopes are observed for the analyzed samples, being higher for the carbon nanotubes (CNT) based samples. The results suggest that the active sites participating in the gasification reaction can be catalytic sites for ORR although the specific catalytic activity is determined by the carbon structure. Thus, active sites in CNT show higher activities toward ORR and carbon gasification reactivities than others.

1. Introduction

Fuel cells (FC) convert chemical energy of fuel and oxidant into electric energy. Unlike batteries, they do not need recharging as long as fuel and oxidant are continuously supplied [1]. At the cathode of a proton exchange membrane fuel cell, oxygen is reduced by reaction with protons and electrons to produce water ($1/2O_2 + 2H^+ + 2e^- \rightarrow H_2O$) [1]. The sluggish reaction kinetics of Oxygen Reduction Reaction (ORR) even on the best Pt-based catalyst requires high Pt loading (~0.4 mg cm^{-2}) to achieve a desirable fuel cell performance. Pt is a scarce and expensive metal and the Pt-based electrodes suffer from CO deactivation [2–5]. Hence, cathode development requires special attention to find the best catalyst and electrode structure to combine performance and stability [3]. Indeed, heteroatom (N, S, P, B and F)-doped carbon materials, transition metal oxides (e.g., CoO, Co_3O_4, Cu_2O, MnO_2) and metal nitrogen complexes (Co-Nx, Fe-Nx) on carbon nanomaterials can be promising candidates as non-precious metal catalysts for ORR in alkaline medium [6–8]. Because of its desirable electrical and mechanical properties as well as large accessible surface area, new nanostructured carbon materials such as graphene and carbon nanotubes (CNT) have widely contributed to design advanced electrocatalysts [9].

Nowadays, dopants, edges, and defects have been demonstrated to generate promising ORR

activity to metal-free nanocarbon materials by modification of electronic structure of the materials [10]. In the case of nitrogen doping, in general, it is concluded that carbon atoms near nitrogen are the active sites for ORR, although there are discrepancies about the structure of the most active sites [11–14]. Regarding the effect of carbon edges toward ORR, studies using highly oriented pyrolytic graphite by Shen et al. revealed that the activity is much higher at the edge of graphite than at the basal plane [15]. Tang et al. explained using DFT calculations that all-carbon topological defects can deliver an excellent activity for both ORR and OER, while topological defects containing nitrogen doping are expected to produce a higher enhancement [16]. In addition, structure of a nitrogen doped Stone-Wales defect provides active sites and its ORR activity can be tuned by the curvature around the active sites [17]. Defective activated carbon derived via heat treatment of the N-doped activated carbons demonstrated comparable activity to commercial Pt/C catalysts [18]. Combination of the defects or edge carbons and the electron transfer resistance ultimately determines the ORR performance of drilled CNT [19]. In consequence, it was proposed that the origin of ORR activity is a result of carbon restructuring and the possible formation of topological defects during the removal of high temperature CO desorbing functional groups [20].

To sum up, a wide range of metal free carbon based catalysts have been explored for improving

ORR activities in recent years. However, knowledge of the critical active sites and underlying mechanism still remains confusing and controversial [16].

Meanwhile, extensive investigation regarding carbon-oxygen gasification were carried out from which clear evidences about the involved active sites and the reaction mechanism were collected [21,22]. Oxygen-transfer reactions of carbon materials are at the heart of fuel combustion and gasification processes and much progress has been made in achieving their fundamental understanding [23]. As described by reaction (1), in carbon gasification or combustion the oxygen molecule reacts with the carbon reactive site (Cf_1) from the carbon structure forming an intermediate that desorbs as CO or CO_2.

$$O_2 + 2Cf_1 = 2C–O \quad (1)$$

In ORR, it was stablished that the first step in the reduction of oxygen is the one-electron reduction to superoxide ion, as detailed in Reaction (2) [24]

$$O_2 + e^- + Cf_2 = C–O_2* \quad (2)$$

Subsequent to Reaction (2) the adsorbed superoxide anion radical picks up a proton from the electrolyte solution to form and desorb a hydroperoxide ion HO_2^-, thus regenerating the same carbon active site (Cf_2). Radovic has questioned if the sites which are related to carbon gasification (Cf_1) and ORR (Cf_2) are different or not. Answering this question could bring light

to the understanding of the ORR mechanism and in tailoring carbon surfaces [25].

In this sense, the concept of active surface area (ASA), which is derived from the studies of carbon gasification, was extremely useful to understand the reactivity of carbon materials [26]. Reactivity is another extensively used measurement for analyzing the oxidation behavior of carbonaceous solids [27]. The ASA has been recently applied not only to the carbon gasification reactions but also to electrochemical processes [28]. For instance, the value of irreversible capacity of lithium ion batteries or the electrochemical storage of hydrogen are directly related with the ASA [29,30].

In summary, several electrochemical properties have been correlated with ASA. However, the correlations of ORR on carbon materials and carbon-oxygen gasification properties have not been identified. The aim of this study is to elucidate the relationship between carbon-oxygen gasification properties and ORR activities. For this purpose, heteroatoms and metal free carbon materials including different structures and porosities, such as activated carbons, carbon blacks, carbon nanotubes, carbon nanofiber and graphite were selected. After identifying structural and electrochemical properties of these materials, some insights about the mechanism for ORR in relation to carbon-oxygen gasification properties are proposed.

2. Experimental

2.1 Material Preparation

Commercial carbon materials and materials prepared in our laboratory were used in this study. Multi-wall Carbon Nanotubes (MW) with a 99 % of purity, outer diameter: 13-18 nm, length: 3–30 μm and Single-Wall/Double-Wall Carbon Nanotubes (SW) with a 99 % of purity, outer diameter: 1-2 nm and length: 3–30 μm were purchased from Cheap Tubes Inc. (Brattleboro, Vt, USA). Carbon nanotube herringbone (labeled as Herring along this work) from TOKYO CHEMICAL INDUSTRY with a 95 % of purity, outer diameter: 10-20 nm and length: 5–15 μm was also used. Graphite (KS4) from TIMCAL Ltd., commercial XC-72F Vulcan carbon black (XC72) from Cabot Corporation, CD-6008 carbon black (CB) from COLUMBIAN CHEMICALS and a highly microporous activated carbon (YPF) supplied from KURARAY were also used. A microporous char (AC) derived by carbonization of phenolformaldehyde polymer resin and carbon nanofiber (CNF) synthesized by our lab were used.

It is known that presence of metallic impurities, such as those employed as catalysts in the production of carbon nanotubes, yield high catalytic activities with respect to oxygen reduction reaction [31] and carbon oxidation [32]. For this reason, the analyzed carbon materials were treated by 5 M hydrochloric acid at 50 ˚C overnight to remove the inorganic matter. In addition,

SW treated with concentrated nitric acid at 70 ˚C for 12 h were also prepared [33]. This sample was labeled as SW_HNO_3. The resulting samples were filtered and washed several times by distilled water until the pH of the filtrate was the same as that of the distilled water. Finally, the materials were dried at 120 ˚C, what was followed by physicochemical and electrochemical characterizations for analyzing the purity of the samples.

2.2 Physicochemical characterization

Transmission electron microscopy (TEM) images of the materials were taken with a JEOL JEM-2010 microscope operated at 200 kV. The samples were suspended in ethanol to obtain a homogeneous dispersion before drop-casting them on a copper grid and then placed in the measurement chamber. Porous texture of all the samples were determined by physical adsorption (N_2 at -196 ˚C and CO_2 at 0 ˚C) using an automatic adsorption system (Autosorb-6, Quantrachrome) after samples out-gassing at 250 ˚C under vacuum for 4 h. The total micropore volume (pore size smaller than 2 nm) was calculated from the application of the Dubinin–Radushkevich theory to the N_2 adsorption at -196 ˚C. The narrow micropore volume (pore size smaller than around 0.7 nm) has been assessed from CO_2 adsorption at 0 ˚C using the DR equation [34,35]. The densities of the adsorbed phase used for the calculations were 0.808 and 1.023 g ml^{-1} for N_2 and CO_2, respectively. The apparent specific surface area was calculated

by the BET equation.

2.3 Carbon-oxygen gasification characterization

The severity of thermal treatment conditions (such as residence time, temperature and heating-rate) during the carbon-oxygen reaction measurements have a significant effect on the ASA as well as reactivity [36]. Therefore, all of the purified carbon samples were treated by same thermal treatment conditions. The ASA gives a measurement of the number of reactive carbon atoms or carbon active sites corresponding mainly to edge planes and defects of a carbon sample [29]. The ASA of our samples was measured using an established method which is based on di-oxygen chemisorption [37]. Firstly, about 10 mg of purified samples were heat treated up to 920 ˚C at a heating rate of 20 ˚C min^{-1}, flow rate of 100 mL min^{-1} and kept at 920 ˚C for 0.5 h under N_2 to remove oxygen complexes on the carbon surface. Afterwards, temperature is lowered to 250 ˚C and kept for 1 h while keeping the inert atmosphere. Next, synthetic dry air (20 vol.% O_2 in N_2) is fed to the thermobalance for 7 h to perform the oxygen chemisorption step. The ASA was then determined from the weight uptake of the samples by the following equation assuming that each chemisorbed oxygen atom occupies an area of 0.083 nm^2 [37].

$$ASA = \frac{1}{w_0} \cdot \frac{A \times n \times (w_c - w_0)}{N_O} \qquad (3)$$

where A is the area that one oxygen atom occupies per edge carbon atom, n is Avogadro constant, w_0 is the starting weight of carbon in the chemisorption step, w_c is the weight of carbon after oxygen chemisorption and N_O is oxygen atomic weight.

Reactivities for carbon-oxygen gasification were determined by isothermal TGA analysis under synthetic dry air. About 10 mg of the purified samples were heated in a N_2 stream up to 920 ˚C at a rate of 20 ˚C min^{-1} and kept for 0.5 h. Next, temperature is lowered to the selected reaction temperature (typically from 500 ˚C to 670 ˚C) and kept for 1 h. Finally, synthetic dry air is fed, and the resulting weight changes were recorded continuously as a function of time. The reactivity was given by the following equation

$$R_T = -\frac{1}{w_0} \cdot \frac{dw}{dt} \qquad (4)$$

Where R_T is the initial reactivity at a temperature T ($gg^{-1}h^{-1}$), w_0 is the initial mass of the sample (g), on an ash free basis, and $\frac{dw}{dt}$ is the initial rectilinear weight loss rate (gh^{-1}) [32]. A TA thermobalance (SDT 600) with a sensitivity of 1 µg has been used for these measurements.

2.4 Surface chemistry

Temperature-Programmed Desorption (TPD) measurements are extensively used for characterizing the surface functionalities of carbon materials [38,39]. Oxygen complexes decompose mostly as CO_2 and CO that are followed by TPD techniques [40]. TPD experiments

were performed in a thermogravimetric system (TA Instruments, SDT Q600 Simultaneous) coupled to a mass spectrometer (Thermostar, Balzers, BSC 200). The samples were heat treated up to 920 ˚C at a rate of 20 ˚C min^{-1} followed by keeping this temperature for 0.5 h under a Helium flow rate of 100 mL min^{-1} to clean the carbon surfaces. The CO and CO_2 evolving from the samples during the heat treatment was monitored (TPD experiment). TPD experiments were also done for the samples after the heat treatment process (HT-TPD). Amounts of CO and CO_2 desorbed from the samples during the experiments were quantified by calibration of 28 and 44 m z^{-1} signals using calcium oxalate.

Furthermore, the surface composition of the catalysts was investigated by X-ray photoelectron spectroscopy (XPS) in a VG-Microtech Multilab 3000 spectrometer, equipped with an Al anode.

2.5 Electrochemical characterization

Electrochemical activity tests towards ORR were carried out at 25 ˚C in a three-electrode cell with 0.1 M KOH electrolyte using a Autolab PGSTAT302 (Metrohm, Netherlands) potentiostat, a graphite bar as counter electrode and Reversible Hydrogen Electrode (RHE) electrode introduced in the working solution as reference electrode. A rotating ring-disk electrode (RRDE, Pine Research Instruments, USA) equipped with a glassy carbon (GC) disk (5.61 mm

diameter) and an attached Pt ring was used as working electrode. Since this study aims to get information about carbon active sites and to compare with ASA and carbon-oxygen reactivity data, all the samples used in this evaluation were also heat treated at 920 ˚C for 0.5 h under N_2 to remove the surface oxygen complexes as it was done for ASA and reactivity measurements. After this thermal treatment the samples were immediately characterized for ORR to minimize the influence of contact with the atmosphere. We have checked that the ORR activity is not modified when the annealed samples remain in contact with air for periods ranging from a few hours to a few days. In addition, a measurement done by protecting the heated sample in inert atmosphere was carried out with a highly microporous activated carbon (YPF) which contains relatively large amounts of edge sites and the results were not different to those in unprotected conditions. The samples were dispersed in a solution of 20 vol.% of isopropanol, 80 vol.% of water and 0.02 wt.% of Nafion@ (the weight ratio of Nafion@ to carbon sample is 1:5) to prepare a final dispersion of 1mg ml^{-1} of the carbon material. Typically, 100 µl of the dispersion was pipetted on the GC disk electrode (carbon sample loading of 400 µg cm^{-2}) to obtain uniform catalysts layer for ORR study. The sample on the GC was dried by heating lamp for evaporation of the solvent. Cyclic Voltammetry (CV) and linear sweep voltammetry (LSV) were carried out from 1 to 0 V (vs. RHE). The CV was performed in both N_2 and O_2 saturated

atmosphere at 5 and 50 mV s^{-1}. The LSV was done in an O_2-saturated atmosphere for 1600 rpm at 5 mV s^{-1}. LSVs of ORR were corrected for the capacitive current contribution, which was obtained from CV under N_2 at 5 mV s^{-1}. The potential of the Pt ring electrode was kept at 1.5 V (vs. RHE) and its current was also measured during the LSV measurement. The electron transfer number (n) of ORR on the catalysts modified electrode was determined by the following equation.

$$n = \frac{4 \times Id}{Id + Ir/N} \qquad (5)$$

where *Id* is disk current, *Ir* is ring current, and N is the collection efficiency of the ring which was experimentally determined to be 0.37.

3. Results and Discussion

3.1 TEM images

TEM observations were carried out to get information about the carbon structure on a microscopic scale. The TEM images for KS4, XC72, CB, CNF, MW, Herring and SW are displayed in Fig. 1. TEM images for YPF and SW_HNO_3 are presented in Fig. S1. Highly developed and stacked structures of 002 lattice fringes, which are typical of graphitic materials, are observed for KS4, Fig. 1a. For carbon black samples, namely XC72 and CB, nanosized spherical amorphous particles of different sizes are observed in TEM images, Fig. 1b, c, being

smaller for CB. This feature delivers more voids spaces (which could determine the porous texture of carbon blacks) between the nanosized particles on CB sample. Hence, larger BET surface area of CB than XC72 is measured as explained later in Table 1. CNF presented a disordered structure with fibril nanotexture (highlighted by white arrow), Fig. 1d. TEM image of AC illustrates the amorphous carbon structure which was previously studied [40], Fig. 1e. Finally, for carbon nanotube samples, different structures are observed. First, TEM of multiwalled carbon nanotubes (MW) shows that the graphite planes of the MW walls are parallel to the axis of the nanotube, Fig. 1f. Second, herringbone nanotubes (Herring) shows its characteristic nanostructure where the graphite planes forming the walls are most of them stacked forming an angle close to 45º with the axis of the tube Fig. 1g. Contrarily, single walled carbon nanotubes (SW) presented bundles of very thin carbon nanotubes, Fig. 1h. The diameter of nanotubes follows the order of Herring > MW > SW, in close agreement with their specific surface area values (Table 1).

TEM images indicate that samples selected in this study have very different structures. The ordered, spherical particle and tube type structures of carbon materials are observed for KS4, XC72, MW, Herring and SW. In contrast, AC, CB, YPF and CNF displayed highly disordered carbon structure.

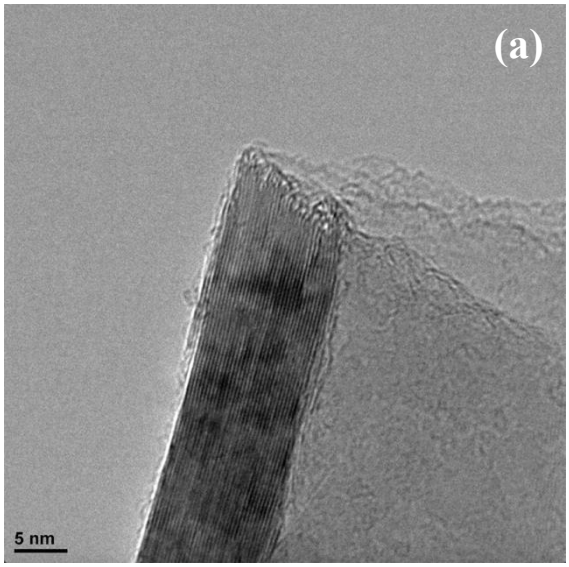
(a)
5 nm

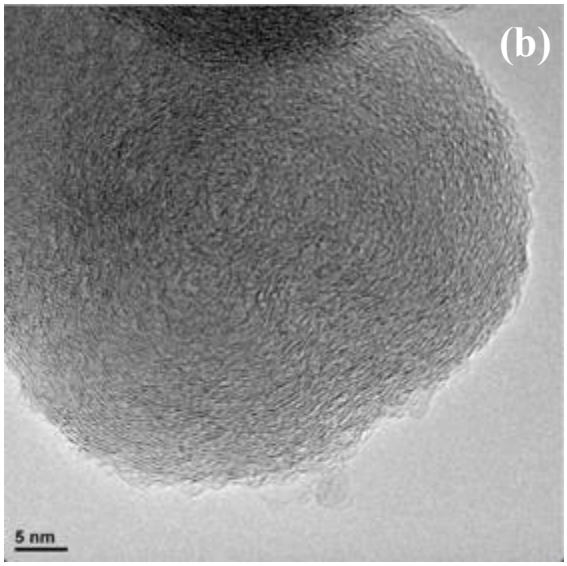
(b)
5 nm

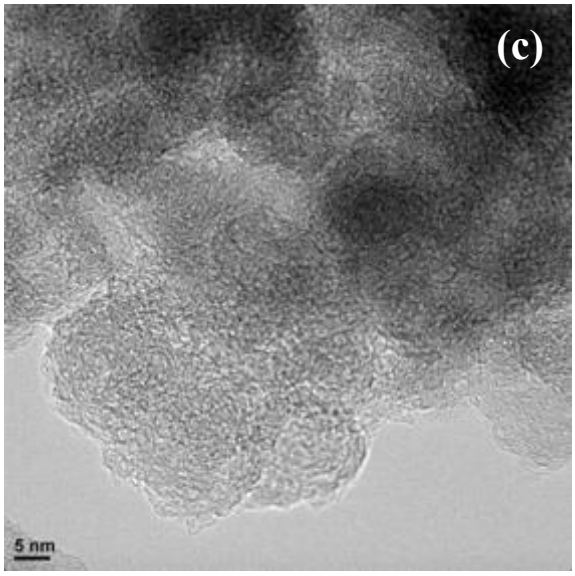
(c)
5 nm

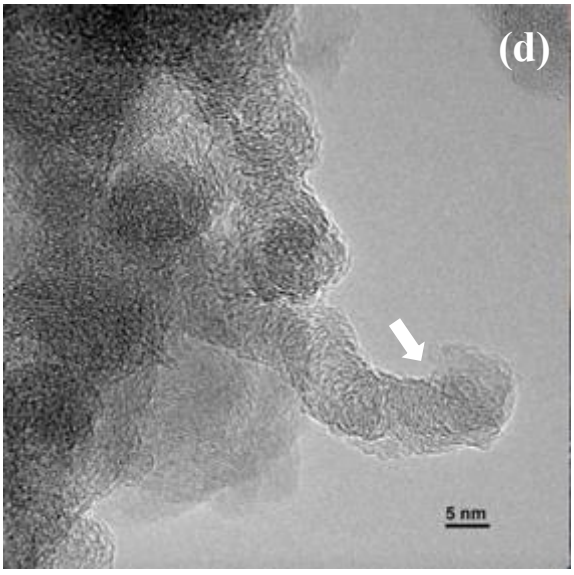
(d)
5 nm

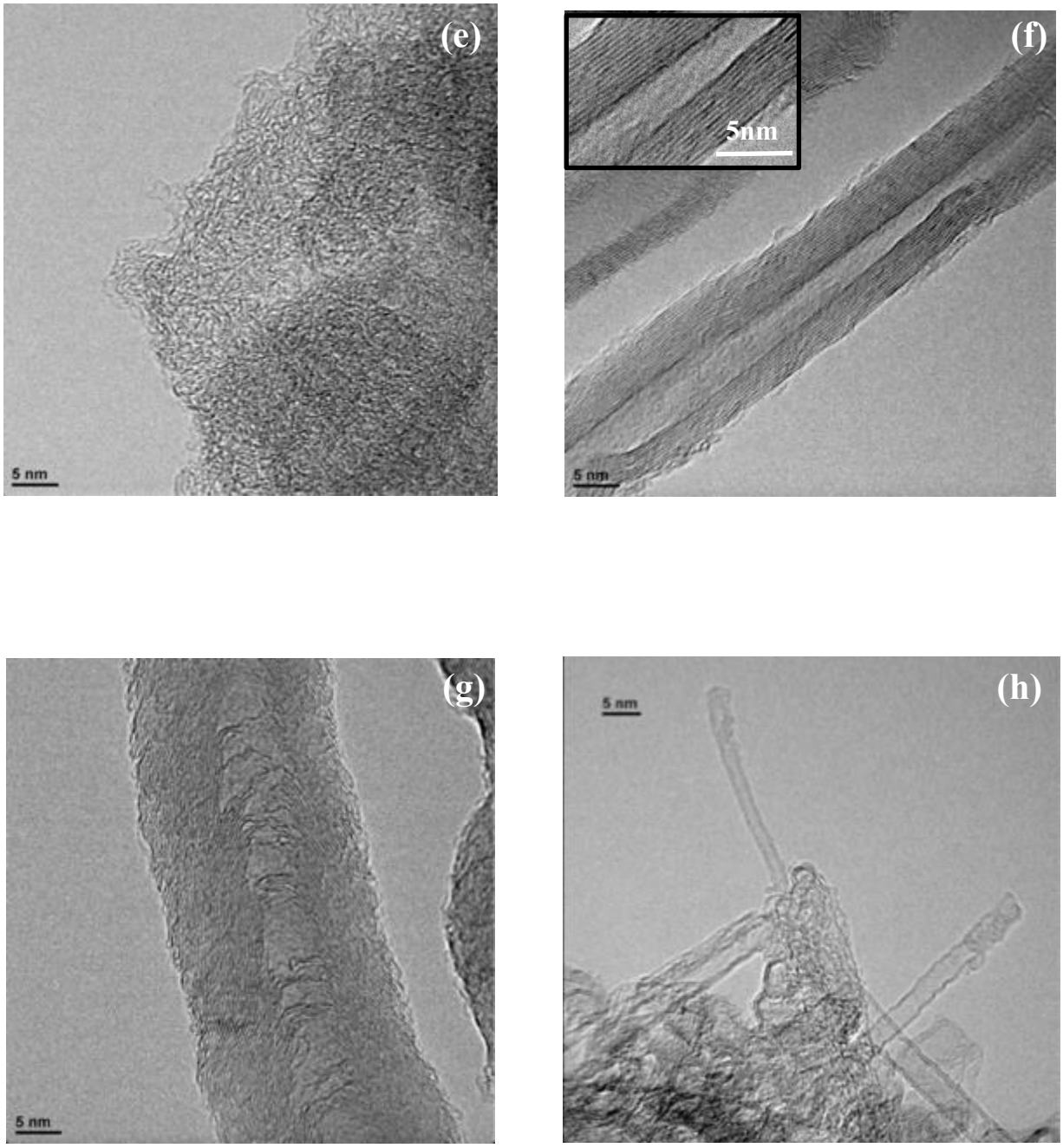

Fig. 1. TEM images of (a) KS4, (b) XC72, (c) CB, (d) CNF, (e) AC, (f) MW, (g) Herring and (h) SW. The arrow indicates the location of fibril structure. All samples were heat treated at 920 ˚C for 0.5 h under N_2 before the analysis.

3.2 Thermogravimetric analysis

The inorganic matter content of the samples prepared in this work was analyzed by TGA under synthetic air. Fig. S2 shows the TG curves of non-CNTs (KS4, XC72, CB, CNF and AC) and CNTs based samples (MW, Herring, SW and SW_HNO_3). The TG weight loss indicated that the samples have a carbon content higher than 99.8% and 98.8% for non-CNTs and CNTs based samples, confirming that most of the metal content was removed by our purification procedures. The possible contribution of residual metal impurities toward ORR is explained in ORR measurements section.

3.3 Characterization of surface chemistry

Fig. 2 shows the CO_2 and CO gas evolution profiles during TPD for all the carbon samples before and after heat-treatment at 920 ˚C for 0.5 h in He atmosphere, respectively. By comparing the TPD profiles between Fig. 2 (a), (b) and Fig. 2 (c), (d), removal of most of oxygen complexes on the carbon surface can be confirmed by the thermal treatment at 920 ˚C. Hence, the effect of oxygen functionalities on the carbon surface toward ORR activity should be negligible for our prepared carbon samples [41,42]. Nevertheless, the very small peaks observed for samples Herring and CNF at ca. 600 ºC can be related to traces of metal still present in these samples.

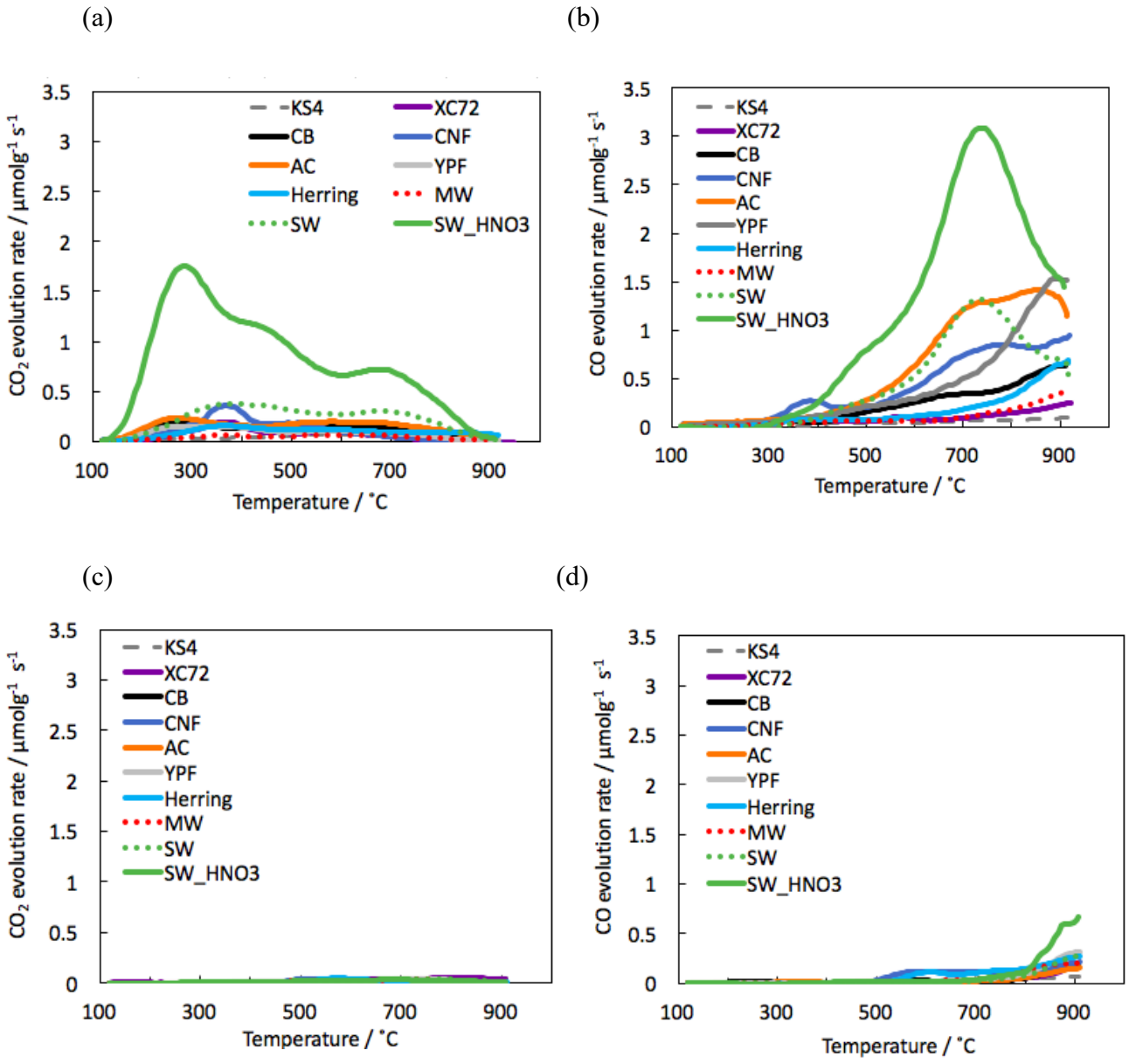

Fig. 2. Gas evolution profiles in He before (a) CO_2 (b) CO and after (c) CO_2 (d) CO heat treatment at 920 ˚C for 0.5 h of the carbon samples up to 920 ˚C at rate of 20 ˚C min^{-1}

In addition, XPS spectra of the heat treated samples show the presence of C 1s and O 1s emissions (Fig. S3). None of the high-resolution XPS spectra reveal the presence of other heteroatoms like nitrogen, phosphorus, halogens, etc. (Fig. S4). The surface chemistry characterized by TPD and XPS for the samples is summarized in Table S1.

3.4 Porous texture and carbon-oxygen gasification properties

N_2 adsorption isotherms at -196 ˚C and CO_2 adsorption isotherms at 0 ˚C have been determined in all the samples to characterize their porous textures (Fig. S5 contains the nitrogen isotherms of the samples). Table 1 compiles the BET surface area (S_{BET}), micropore volume (V_{DR}^{N2}) and narrow micropore volume (V_{DR}^{CO2}) calculated from N_2 and CO_2 adsorption for each sample. It can be seen that the materials have different porous texture. Specific surface areas ranged from 36 $m^2\,g^{-1}$ (sample KS4) to more than 1700 $m^2\,g^{-1}$ (sample YPF). XC72, CNF and MW presented similar S_{BET} (196 ~ 287 m^2g^{-1}). CB, AC and SW showed intermediate S_{BET} values (580 ~ 600 $m^2\,g^{-1}$).

Table 1 also contains the values of ASA and reactivity for carbon-oxygen reaction measured under synthetic dry air at 250 ˚C and 550 ˚C, ASA and R_{550}, respectively. ASA is related to the structural ordering of the carbon materials [43]. Edge plane on carbon surface include all types

of defects that could be present in the carbon structures (stacking faults, single and multiple atom vacancies, dislocations, etc) which constitute ASA [26,44]. Therefore, generally ordered structures have low amount of edge sites whereas undeveloped structures contain higher concentration of edge site which are responsible for dissociative oxygen chemisorption, and thus leading to high ASA. For our prepared samples, KS4, XC72, CB and CNTs based catalysts display relatively low ASA (<14 m^2 g^{-1}). On contrast, AC, CNF and YPF which showed disordered carbon structures as revealed in Fig. 1, have higher ASA values (> 20 m^2 g^{-1}). Moreover, Table 1 reveals that nitric acid oxidation of SW affects their porous texture (note the enhancement of S_{BET}, V_{DR}^{N2} and V_{DR}^{CO2}). Furthermore, SW_HNO_3 showed higher ASA and reactivity than SW which might be due to the formation of structural defects during the wet oxidation of SW_HNO_3 [33,43]. Table 1 depicts that S_{BET}, V_{DR}^{N2}, and V_{DR}^{CO2} are not the factors determining ASA and R_{550} for non-CNTs. On the other hand, ASA and R_{550} might be related to S_{BET} for CNTs based samples, suggesting that these samples share common structural features that are different to those of the others.

Table 1 Porous texture, ASA and R_{550} of the selected samples

Sample*	S_{BET} / $m^2\ g^{-1}$	V_{DR}^{N2} /$cm^3\ g^{-1}$	V_{DR}^{CO2} /$cm^3\ g^{-1}$	ASA /$m^2\ g^{-1}$	R_{550} /$g\ g^{-1}\ h^{-1}$
KS4	36	0.01	--	0.5	0.06
XC72	254	0.10	0.05	4.7	0.74
CB	583	0.26	0.17	14.0	1.14
CNF	287	0.11	0.07	28.9	1.99
AC	593	0.24	0.26	36.7	2.16
YPF	1757	1.24	0.48	26.4	2.20
Herring	**123**	**0.05**	**0.03**	**2.2**	**0.47**
MW	**196**	**0.07**	**0.02**	**2.8**	**2.00**
SW	**587**	**0.21**	**0.13**	**6.1**	**2.39**
SW HNO_3	**976**	**0.35**	**0.17**	**9.4**	**2.91**

*All samples were heat treated at 920˚C for 0.5h under N_2 before the analyses.

Fig. 3 illustrates the Arrhenius plots (rate vs. 1/T) [45] for the carbon gasification with oxygen obtained in this study. The activation energies in air for the samples were calculated from the slope in Fig. 3 obtaining values between 60 kJ mol^{-1} and 249 kJ mol^{-1}, that are similar to those previously reported [22]. Thermogravimetric profiles of the samples at 480˚C, 500˚C, 530˚C and 550˚C under synthetic dry air are presented in Fig. S6, Fig. S7, Fig. S8 and Fig. S9.

Literature provides evidences of ASA being a better descriptor of gasification reactivity than S_{BET}. According to K.H. van Heek et al., good correlations between ASA and reactivity toward air and steam could be established for different chars and hydropyrolysis chars [46]. Additionally, a positive correlation between ASA and reactivity for a series of demineralized coal chars, PVDC chars and electrode carbon gasified in CO_2 was found [47]. In accordance to these previous results, we have observed a good correlation between ASA and reactivity (R_{500}, R_{530} and R_{550}) for our demineralized carbons (Fig. 4). Interestingly, the slope of the plot of reactivity versus ASA for CNTs based samples is higher than that for non-CNTs based samples, independently of the chosen temperature for R determination.

Since O_2 dissociation step on CNT is predicted to be more exothermic and spontaneous than on its graphene counterpart [48], the higher reactivities of CNTs based samples could be due to their unique structure. Ebbesen et al. investigated the oxygen gasification of carbon

nanotube-containing materials in air and reported that the strong local curvature and imperfect geometry and/or the presence of five-membered carbon rings increase the reactivities of nanotubes [49]. Yao et al. concluded that oxidation of carbon nanotubes is influenced by curvature, pentagon and heptagon rings, and probably helicity [50]. The helicity is an additional factor for nanotubes which implies the existence of relatively exposed steps with high chemical potential where oxidation may occur preferentially. More specifically, the authors mentioned that a smaller tube diameter increases the curvature of the tube walls and the strain of the pentagons at the tip [50]. Thus, nanotubes with smaller diameter begin to oxidize first than those with higher diameter. From the thermodynamic analysis of O_2 adsorption on armchair and zigzag nanotubes, decreasing trend in the thermodynamic parameters with increasing CNT diameter were also obtained [48]. Then, the high reactivities of SW and SW_HNO_3 samples could be explained by their smaller diameters (1~2 nm). Morishita et al. studied the gasification behavior of MWCNTs [51,52]. The changes of appearance of a MWCNTs in the initial stage of gasification were evaluated by a fixed point TEM observation. These TEM images indicated that the gasification occurred preferentially at the structural defects in the MWCNTs rather than at the strain points of the topological defects [51,52]. Since SW_HNO_3 contain more defects sites than SW, the reactivity of SW_HNO_3 is higher than that of SW.

In summary, CNT based carbon samples show higher reactivities than non-CNT based catalysts despite their lower ASA (< 9.4 m^2 g^{-1}). As aforementioned, ASA can be considered as a measure of the number of active sites for carbon gasification in a carbon sample. Then, it could be concluded that the intrinsic activity (i.e intrinsic kinetic constant) for carbon gasification of the active sites on CNT is higher than those of non-CNT samples.

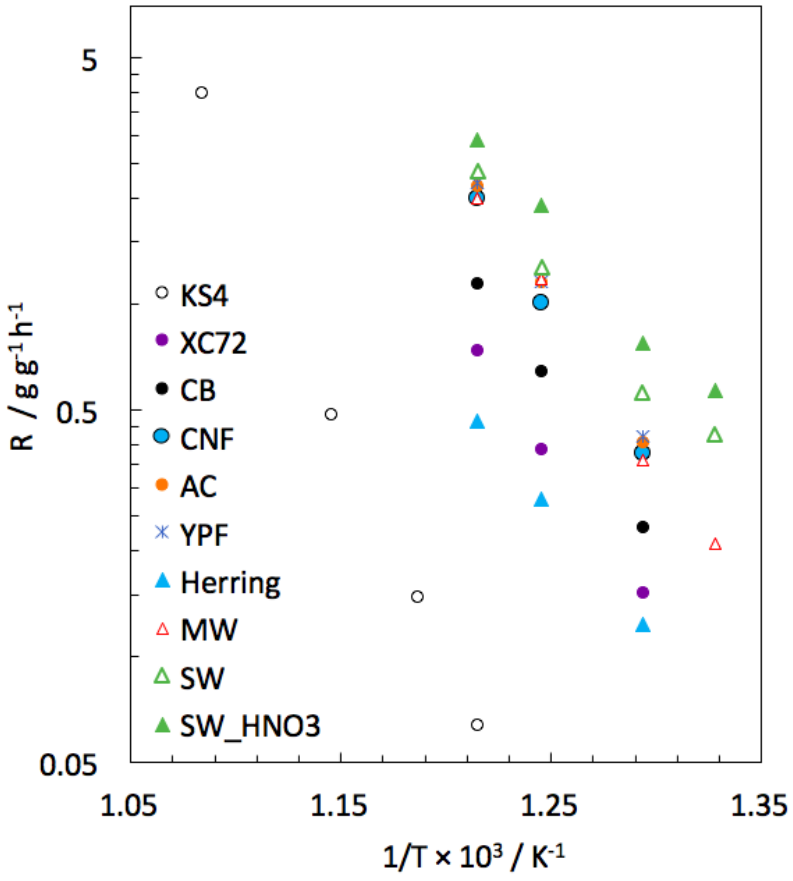

Fig. 3. Arrhenius plots of reactivity for different carbon materials

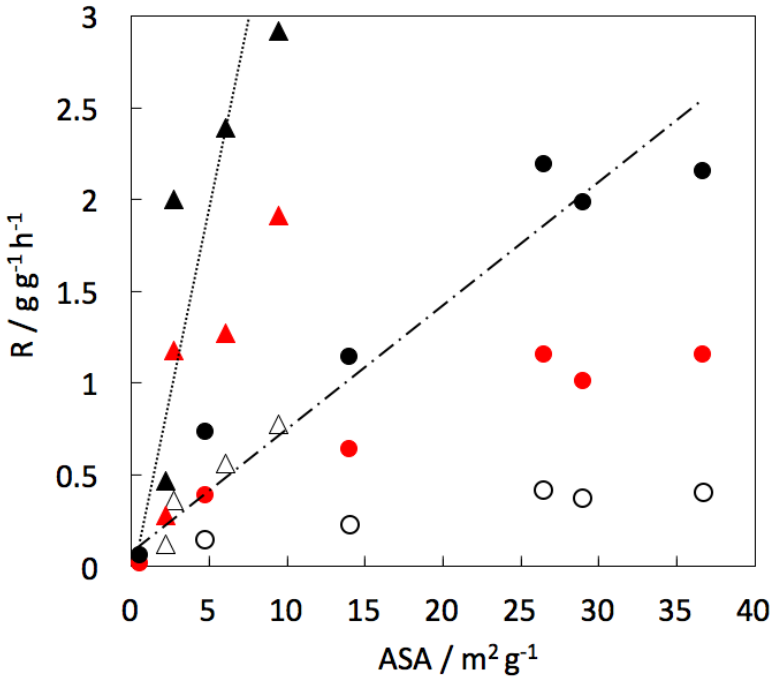

Fig. 4. Relationship between ASA_{250} and R_{500} (white dot), R_{530} (red dot) and R_{550} (black dot) for prepared samples. Triangle dot: CNT based samples (Herring, MW, SW and SW_HNO_3). Circle dot: non-CNT based samples (KS4, XC72, CB, CNF, AC and YPF).

3.5 Electrochemical characterization

Fig. 5 shows the voltammograms in N_2 saturated 0.1M KOH between 0 and 1 V at 50 mVs^{-1} of the samples that were previously heat-treated at 920˚C under N_2. All the voltammograms have a quasi-rectangular shape which are typical of carbon materials where the capacitance is determined by electric double layer formation [53]. Gravimetric capacitance of the electrodes has been determined from the area inside the CVs (2, 14, 49, 33, 53 and 90 F g^{-1} for KS4, XC72,

CB, CNF, AC and YPF, respectively, and 14, 8, 46 and 60 F g^{-1} for MW, Herring, SW and SW_HNO_3, respectively). It is found that the double layer capacitance of these materials are related to the S_{BET}, Table 1.

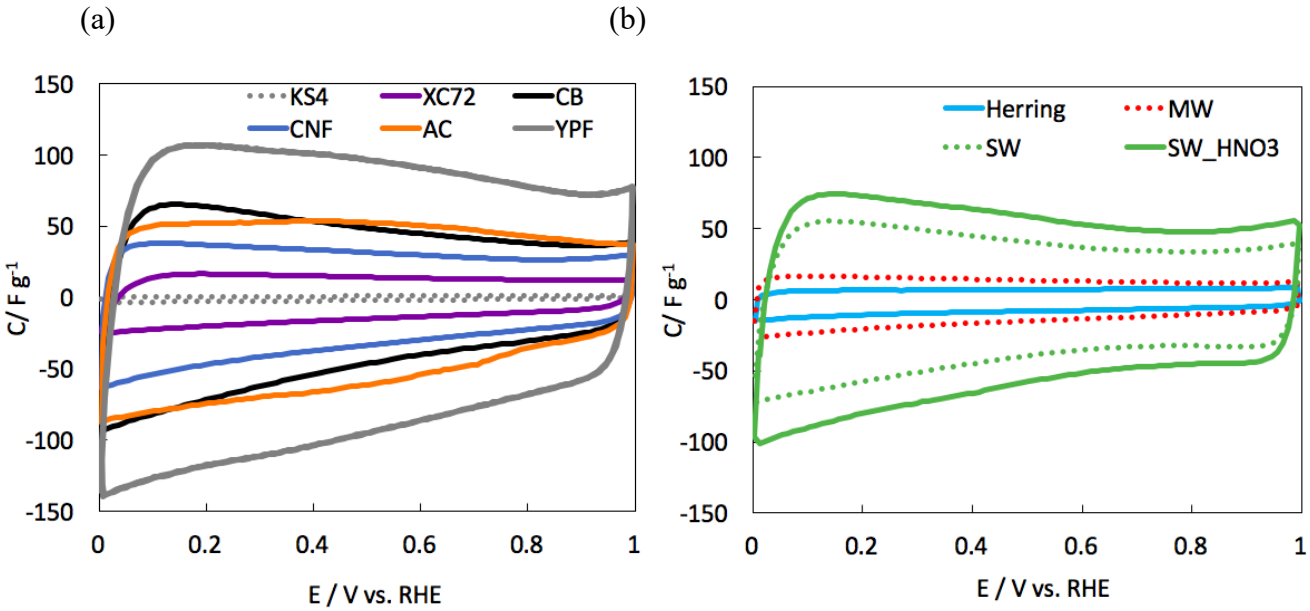

Fig. 5. Steady state cyclic voltammograms for (a) KS4, XC72, CB, CNF, AC, YPF and (b) Herring, MW, SW, SW_HNO_3 in deoxygenated (solid line) 0.1 M KOH solution at 50 mV s^{-1} respectively. sample loading is 400 µg cm^{-2}.

3.6 Oxygen Reduction Reaction measurements

The ORR activity for all the samples was determined by measuring LSVs experiments between 1 and 0 V at an electrode rotating rate of 1600 rpm in O_2-saturated 0.1M KOH. The shape of the recorded curves shows a two-wave electrocatalytic process, the first one starting at potentials around 0.80-0.95V, and the second one ca. 0.4V, Fig. S10. H_2O_2 electrochemical reduction experiments done is our previous study manifested that H_2O_2 produced from oxygen reduction reaction is subsequently reduced, and the intensity and onset potential of the second wave is positively related to the amount of microporosity [54]. This process is out of the scope of this work. In this sense, Fig. 6 shows the LSV in the kinetically controlled O_2 reduction reaction region and the beginning of the diffusional control region (i.e., potential region between 0.4 and 1V). The ORR activity of a 20 wt.%Pt/Vulcan commercial catalyst and the limiting current for oxygen reduction through 2 and 4 e^- reaction pathways obtained from the Levich theory [55] (2.9 and 5.8 mA cm^{-2}, respectively) at 1600 rpm are also plotted. For the analyses of the number of electrons transferred, Fig. 6 c and d, potentials between 0.4 at 0.75V were selected.

In order to compare ORR activity, current densities have been determined at 0.7 V for all samples within the kinetically controlled O_2 reaction region. The current density, number of electrons determined at 0.7 V and onset potential measured at -0.1 mA cm^{-2} on the LSV curves

are summarized in Table S2. SW_HNO_3 has the highest current density as well as *n* while KS4 showed the lowest values. In general, CNT based samples exhibited higher ORR activities (current density and n) than those of non-CNT based samples. It must be noted that if a very low amount of metal content in SW could be improving ORR activity, the activity of SW_HNO_3 should then be inferior to SW. However, the opposite is observed, which suggests that the residual metal impurities are not playing a relevant role toward ORR measurements herein reported. Enhancement of ORR activity for SW_HNO_3 could be correlated with possible formation of topological defects due to the removal of high temperature CO desorbing groups [20]. Moreover, the current density reached in diffusion control for CNTs based samples is higher than 2.9 mA cm^{-2} (i.e. ORR through 2e- mechanism) (Fig. 6a). Since *n* does not reach 4 e-, Fig. 6c, the current densities recorded for CNT based samples could be the result of the combination of different active sites that catalyze ORR through $2e^-$ and $4e^-$ electron transfer pathways. This points out that active sites that are able to catalyze ORR to water through 4 e^- reaction pathways are found in the surface of these samples and its concentration seems to be higher for sample SW-HNO_3.

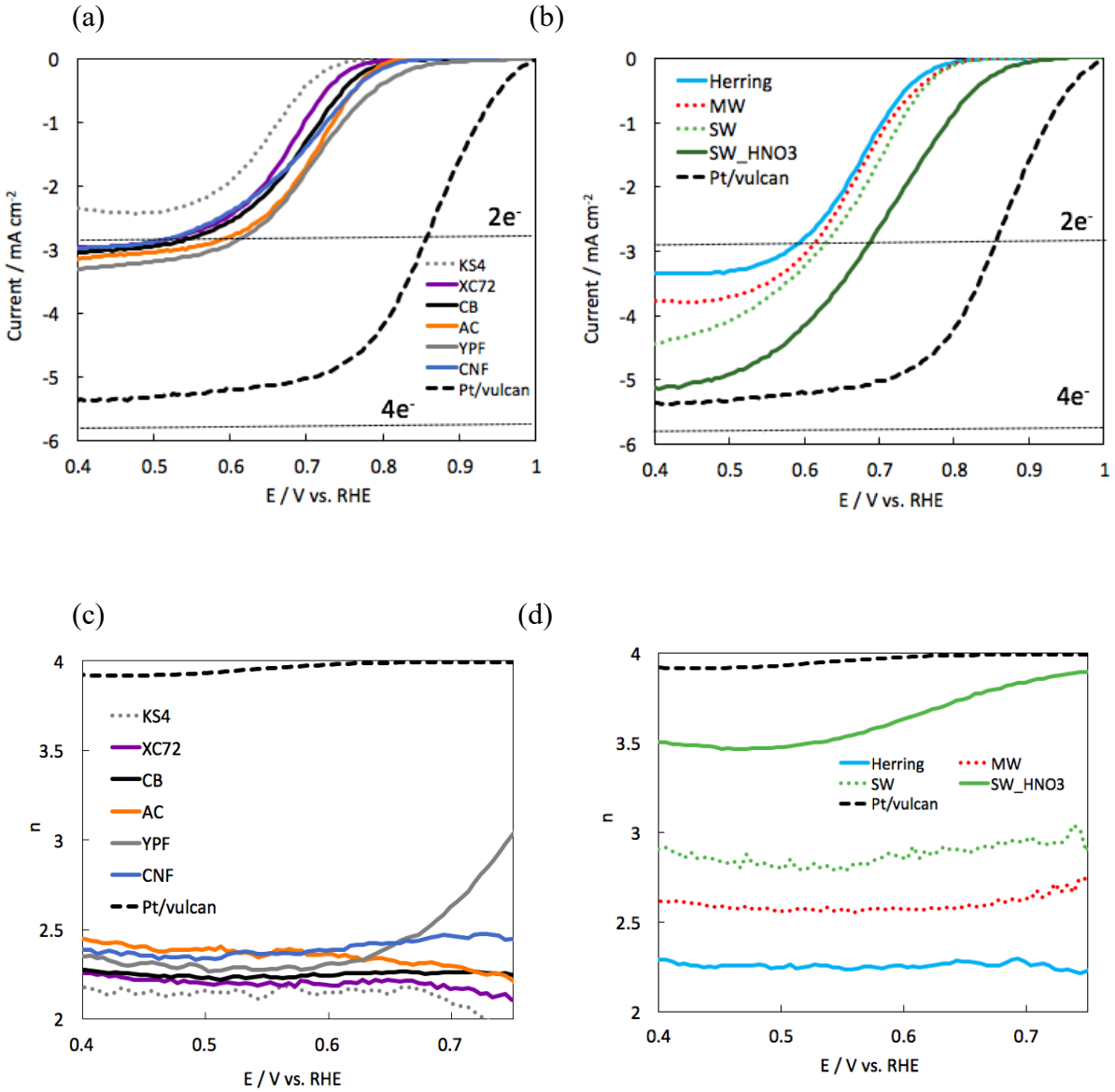

Fig. 6. LSVs during ORR on the disk electrode for (a) KS4, XC72, CB, AC, YPF, CNF and (b) Herring, MW, SW, SW_HNO_3 and number of electrons (n) of the (c) KS4, XC72, CB, AC, YPF, CNF and (d) Herring, MW, SW, SW_HNO_3 in O_2 - saturated 0.1 M KOH solution at 1600 rpm with a sweep rate of 5 mV s^{-1} respectively. Sample loading is 400 µg cm^{-2}. All the samples were heat treated at 920 ˚C for 0.5 h under N_2 before this ORR activity measurement. The values of Pt/Vulcan are included as reference.

To deepen into the relationship between carbon-oxygen gasification properties and ORR activities, the current density and *n* measured at 0.7 V versus ASA250 and R_{550} are compared in Fig. 7 and Fig. 8, respectively.

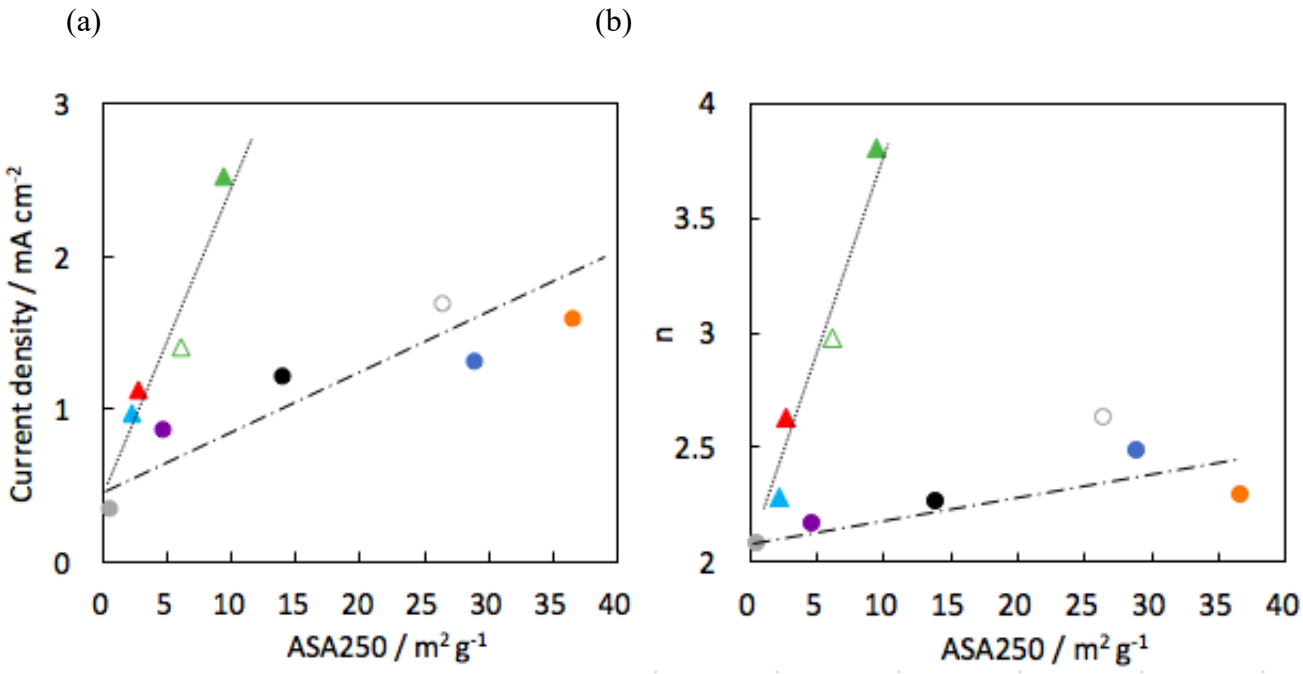

Fig. 7. ASA dependence of (a) Current density and (b) n measured 0.7V in O_2 – saturated 0.1M KOH solution at 1600rpm. △: CNT based samples (MW, SW, SW_HNO_3 and Herring). ◯: rest of samples (KS4, XC72, CB, CNF, AC and YPF). Sample loading is 400 μg cm^{-2}.

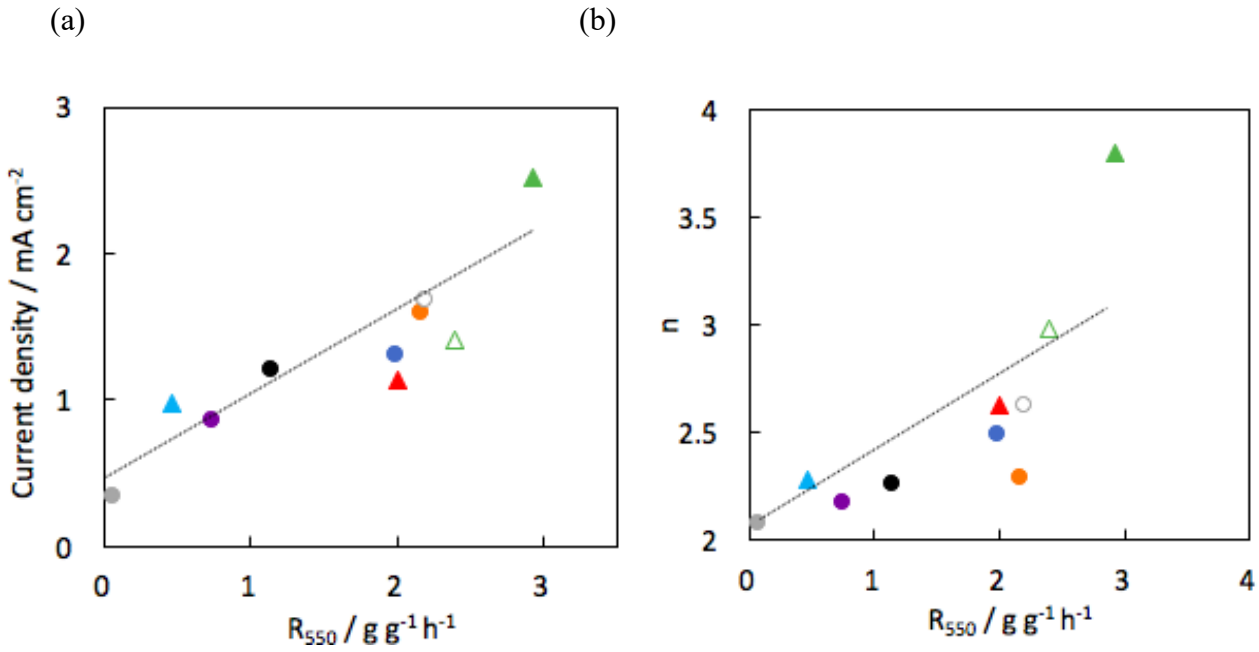

Fig. 8. R_{550} dependence of (a) current density and (b) n measured at 0.7V in O_2 – saturated 0.1M KOH solution at 1600rpm. △: CNT based samples (MW, SW, SW_HNO_3 and Herring). ◯: the other samples (KS4, XC72, CB, CNF, AC and YPF). Sample loading is 400 μg cm^{-2}.

In general, the ORR current density and *n* increase with ASA, Fig. 7, indicating that the carbon edge sites measured by ASA are the active sites with higher activity for ORR. It is known that the electrode kinetics on the basal plane is slower than on edge planes sites (around 7 orders of magnitude slower) [56]. Besides, there are several reports which illustrated that edge carbon atoms are able to improve ORR activity. Ball-milled graphite and CNT with more exposed

edges showed significantly improved ORR activity [13]. Gara et al. prepared basal plane pyrolytic graphite (BPPG) electrodes and edge plane pyrolytic graphite (EPPG) electrodes [56]. BPPG electrodes are cut so as to expose the hexagonal plane of the graphite layer while EPPG is cut perpendicular to BPPG, so as to expose as many graphite sheet ends as possible. It was demonstrated that the current for ORR on the EPPG was superior due to a large number of edge sites containing higher activity toward ORR [56]. Interestingly, as previously observed for the reactivity experiments in Fig. 4, the slope relating ORR current density and ASA is higher for CNTs based samples than that for non-CNTs based samples, Fig. 7.

However, both the current density for ORR and *n* are well described for both set of samples by the carbon gasification reactivity, Fig. 8. This proportional relationship between reactivity and the ORR current density and *n* is manifesting for the first time that carbon gasification reactivity and oxygen reduction reaction share active sites and, at least, some of the starting steps in the reaction mechanism, no matter the porosity and structure of the involved carbon materials.

TEM observations in Fig. 1 showed that the carbon samples possess different structures, while TPD and XPS analysis indicate that all of the samples contain very low amount of surface oxygen complexes and the absence of heteroatoms in their compositions, Table S1. Since

dopants effects for the ORR activities can be discarded, the structural differences could be the factor determining the activities observed. Indeed, the role of structural effects on ORR activities in CNT have been discussed. Zhang et al reported that the curvature effect plays important role in adsorption and reduction of oxygen for CNTs [57]. The limiting potential for ORR can be maximized by tuning the curvature around the active sites of CNT [58]. Bamboo-shaped MWCNT demonstrated superior ORR characteristics to hollow-shaped MWCNT due to the disordered surface with pentagonal defects, rounded compartments, and edge plane sites [59]. CNT walls can modify electronic interaction and diffusion behavior of reactants for further catalytic activities [60]. In this work, the highest ORR activity and gasification reactivity values have been achieved for highly defective SW (i.e., SW-HNO_3), confirming that the combination of large number of edge sites, a high curvature with smaller diameter of the tube and a high electrical conductivity are the most desirable features for the development of the most active carbon materials for ORR.

4. Conclusions

The relationship between ORR activities and carbon-oxygen gasification parameters (ASA and reactivity) were quantitatively identified for materials with different structures. In general, the

ORR activities of carbon materials increase with ASA. However, for a similar ASA value, CNT based samples showed higher ORR activities and carbon gasification reactivities than non-CNT based samples. These results suggest that the active sites on CNT have higher activity toward ORR and carbon gasification. By checking the absence of impurities and the presence of a low amount of surface oxygen groups by TPD and XPS analyses, it was clarified that not only active edge sites measured by ASA but also the structure of carbon materials are the critical factors determining ORR activity and the possibility of enabling a $4e^-$ reaction pathway. The unique features of CNT structure such as a reduced number of graphene layers in their walls and pronounced curvature, especially for those CNTs of smaller diameter, can be responsible for such increase in ORR activity. In addition, ORR activities and carbon gasification reactivity were linearly correlated which suggests that both reactions share the same active sites as well as some steps of the reaction mechanism. It has been found that CNT containing the highest amount of ASA and a low number of graphene layers (as in the case of SW) could be promising materials for designing effective ORR catalysts, what could be potential alternatives for the development practical cathodic materials in FC.

Acknowledgements

The authors gratefully acknowledge the financial support by MINECO (CTQ2015-66080-R MINECO/FEDER) and HEIWA NAKJIMA FOUNDATION.

References

[1] M. Shao, Q. Chang, J.-P. Dodelet, R. Chenitz, Recent Advances in Electrocatalysts for Oxygen Reduction Reaction, Chem. Rev. 116 (2016) 3594–3657. doi:10.1021/acs.chemrev.5b00462.

[2] K. Kakaei, Electrochemical characteristics and performance of platinum nanoparticles supported by Vulcan/polyaniline for oxygen reduction in PEMFC, Fuel Cells. 12 (2012) 939–945. doi:10.1002/fuce.201200053.

[3] M. Winter, R.J. Brodd, What Are Batteries, Fuel Cells, and Supercapacitors?, Chem. Rev. 104 (2004) 4245–4270. doi:10.1021/cr020730k.

[4] N. Daems, X. Sheng, I.F.J. Vankelecom, P.P. Pescarmona, Metal-free doped carbon materials as electrocatalysts for the oxygen reduction reaction, J. Mater. Chem. A. 2 (2014) 4085–4110. doi:10.1039/C3TA14043A.

[5] I. Katsounaros, S. Cherevko, A.R. Zeradjanin, K.J.J. Mayrhofer, Oxygen electrochemistry as a cornerstone for sustainable energy conversion, Angew. Chemie - Int. Ed. 53 (2014) 102–121. doi:10.1002/anie.201306588.

[6] P. Trogadas, T.F. Fuller, P. Strasser, Carbon as catalyst and support for electrochemical energy conversion, Carbon. 75 (2014) 5–42. doi:10.1016/j.carbon.2014.04.005.

[7] A. Gabe, J. García-Aguilar, Á. Berenguer-Murcia, E. Morallón, D. Cazorla-Amorós, Key factors improving oxygen reduction reaction activity in cobalt nanoparticles modified carbon nanotubes, Appl. Catal. B Environ. 217 (2017) 303–312. doi:10.1016/j.apcatb.2017.05.096.

[8] C. González-Gaitán, R. Ruiz-Rosas, E. Morallón, D. Cazorla-Amorós, Relevance of the Interaction between the M-Phthalocyanines and Carbon Nanotubes in the Electroactivity toward ORR, Langmuir. 33 (2017) 11945–11955. doi:10.1021/acs.langmuir.7b02579.

[9] C.H. Choi, M.W. Chung, H.C. Kwon, J.H. Chung, S.I. Woo, Nitrogen-doped graphene/carbon nanotube self-assembly for efficient oxygen reduction reaction in acid media, Appl. Catal. B Environ. 144 (2014) 760–766. doi:10.1016/j.apcatb.2013.08.021.

[10] C. Tang, Q. Zhang, Nanocarbon for Oxygen Reduction Electrocatalysis: Dopants, Edges, and Defects, Adv. Mater. 29 (2017). doi:10.1002/adma.201604103.

[11] T. Xing, Y. Zheng, L.H. Li, B.C.C. Cowie, D. Gunzelmann, S.Z. Qiao, S. Huang, Y. Chen, Observation of active sites for oxygen reduction reaction on nitrogen-doped multilayer graphene, ACS Nano. 8 (2014) 6856–6862. doi:10.1021/nn501506p.

[12] D. Guo, R. Shibuya, C. Akiba, S. Saji, T. Kondo, J. Nakamura, Active sites of nitrogen-doped carbon materials for oxygen reduction reaction clarified using model catalysts, Science (80-.). 351 (2016) 361–365. doi:10.1126/science.aad0832.

[13] J. Quílez-Bermejo, E. Morallón, D. Cazorla-Amorós, Oxygen-reduction catalysis of N-doped carbons prepared via heat treatment of polyaniline at over 1100 °C, Chem. Commun. 54 (2018) 4441–4444. doi:10.1039/C8CC02105H.

[14] J. Quílez-Bermejo, C. González-Gaitán, E. Morallón, D. Cazorla-Amorós, Effect of carbonization conditions of polyaniline on its catalytic activity towards ORR. Some insights about the nature of the active sites, Carbon. 119 (2017) 62–71. doi:10.1016/j.carbon.2017.04.015.

[15] A. Shen, Y. Zou, Q. Wang, R.A.W. Dryfe, X. Huang, S. Dou, L. Dai, S. Wang, Oxygen reduction reaction in a droplet on graphite: Direct evidence that the edge is more active than the basal plane, Angew. Chemie - Int. Ed. 53 (2014) 10804–10808. doi:10.1002/anie.201406695.

[16] C. Tang, H.-F. Wang, X. Chen, B.-Q. Li, T.-Z. Hou, B. Zhang, Q. Zhang, M.-M. Titirici, F. Wei, Topological Defects in Metal-Free Nanocarbon for Oxygen Electrocatalysis, Adv. Mater. 28 (2016) 6845–6851. doi:10.1002/adma.201601406.

[17] G. Chai, Z. Hou, T. Ikeda, K. Terakura, Active Sites and Mechanisms for Oxygen Reduction Reaction on Nitrogen - Doped Carbon Alloy Catalysts: Stone−Wales Defect and Curvature Effect, J. Am. Chem. Soc. (2014) 13629–13640. doi:10.1021/ja502646c.

[18] X. Yan, Y. Jia, T. Odedairo, X. Zhao, Z. Jin, Z. Zhu, X. Yao, Activated carbon becomes active for oxygen reduction and hydrogen evolution reactions, Chem. Commun. 52 (2016) 8156–8159. doi:10.1039/C6CC03687B.

[19] F.P. Guoyu Zhong, Hongjuan Wang*, Hao Yu, Haihui Wang, School, Chemically drilling carbon nanotubes for electrocatalytic oxygen reduction reaction, Electrochim. Acta. 190 (2016) 49–56.

[20] K. Waki, R.A. Wong, H.S. Oktaviano, T. Fujio, T. Nagai, K. Kimoto, K. Yamada, Non-nitrogen doped and non-metal oxygen reduction electrocatalysts based on carbon nanotubes: mechanism and origin of ORR activity, Energy Environ. Sci. 7 (2014) 1950–1958. doi:10.1039/c3ee43743d.

[21] J. Lahaye, J. Dentzer, P. Soulard, P. Ehrburger, Carbon Gasification: The Active Site Concept, in: J. Lahaye, P. Ehrburger (Eds.), Fundam. Issues Control Carbon Gasif. React., Springer Netherlands, Dordrecht, 1991: pp. 143–162. doi:10.1007/978-94-011-3310-4_8.

[22] J. P.L. WALKER, M. SHELEF, R.A. ANDERSON, Catalysis of carbon gasification, Chem. Phys. Carbon Vol 4. 4 (1968) 287–383. doi:10.1063/1.2914601.

[23] F. Vallejos-Burgos, S. Utsumi, Y. Hattori, X. García, A.L. Gordon, H. Kanoh, K. Kaneko, L.R. Radovic, Pyrolyzed phthalocyanines as surrogate carbon catalysts: Initial insights into oxygen-transfer mechanisms, Fuel. 99 (2012) 106–117. doi:10.1016/j.fuel.2012.03.055.

[24] D.T. Sawyer, E.T. Seo, One-Electron Mechanism for the Electrochemical Reduction of Molecular Oxygen, Inorg. Chem. 16 (1977) 499–501. doi:10.1021/ic50168a059.

[25] L.R. Radovic, Surface Chemical and Electrochemical Properties of Carbons, in: F. Beguin, E. Frackowiak (Eds.), Carbons Electrochem. Energy Storage Convers. Syst., Taylor & Francis (CRC Press), Boca Raton, FL, 2010: pp. 163–219.

[26] J. Lahaye, P. Ehrburger, Surface chemistry of carbon: an atomistic approach, Pure Appl. Chem. 61 (1989) 1853–1858. doi:10.1351/pac198961111853.

[27] E. Hippo, P.L. Walker, Reactivity of heat-treated coals in carbon dioxide at 900 °C, Fuel. 54 (1975) 245–248. doi:10.1016/0016-2361(75)90037-X.

[28] T. Ishii, S. Kashihara, Y. Hoshikawa, J.I. Ozaki, N. Kannari, K. Takai, T. Enoki, T. Kyotani, A quantitative analysis of carbon edge sites and an estimation of graphene sheet

size in high-temperature treated, non-porous carbons, Carbon. 80 (2014) 135–145. doi:10.1016/j.carbon.2014.08.048.

[29] M.J. Bleda-Martínez, J.M. Pérez, A. Linares-Solano, E. Morallón, D. Cazorla-Amorós, Effect of surface chemistry on electrochemical storage of hydrogen in porous carbon materials, Carbon. 46 (2008) 1053–1059. doi:10.1016/j.carbon.2008.03.016.

[30] F. Béguin, F. Chevallier, C. Vix, S. Saadallah, J.N. Rouzaud, E. Frackowiak, A better understanding of the irreversible lithium insertion mechanisms in disordered carbons, J. Phys. Chem. Solids. 65 (2004) 211–217. doi:10.1016/j.jpcs.2003.10.050.

[31] L. Wang, A. Ambrosi, M. Pumera, “Metal-free” catalytic oxygen reduction reaction on heteroatom-doped graphene is caused by trace metal impurities, Angew. Chemie - Int. Ed. 52 (2013) 13818–13821. doi:10.1002/anie.201309171.

[32] R.G. Jenkins, S.P. Nandi, P.L. Walker, Reactivity of heat-treated at 500 ° C coals in air, Fuel. 52 (1973) 288–293.

[33] C. Vix-Guterl, M. Couzi, J. Dentzer, M. Trinquecoste, P. Delhaes, Surface Characterizations of Carbon Multiwall Nanotubes: Comparison between Surface Active Sites and Raman Spectroscopy, J. Phys. Chem. B. 108 (2004) 19361–19367. doi:10.1021/jp047237s.

[34] D. Cazorla-Amorós, J. Alcañiz-Monge, M.A. de la Casa-Lillo, A. Linares-Solano, CO2 As an Adsorptive To Characterize Carbon Molecular Sieves and Activated Carbons, Langmuir. 14 (1998) 4589–4596. doi:10.1021/la980198p.

[35] D. Lozano-Castelló, D. Cazorla-Amorós, A. Linares-Solano, Usefulness of CO2 adsorption at 273 K for the characterization of porous carbons, Carbon. 42 (2004) 1233–1242. doi:10.1016/j.carbon.2004.01.037.

[36] L.R. Radović, P.L. Walker, R.G. Jenkins, Importance of carbon active sites in the gasification of coal chars, Fuel. 62 (1983) 849–856. doi:10.1016/0016-2361(83)90041-8.

[37] N.R. Laine, F.J. Vastola, P.L. Walker, THE IMPORTANCE OF ACTIVE SURFACE AREA IN THE CARBON-OXYGEN REACTION [1,2], J. Phys. Chem. 67 (1963) 2030–2034. doi:10.1021/j100804a016.

[38] Y. Otake, R.G. Jenkins, Characterization of oxygen-containing surface complexes created on a microporous carbon by air and nitric acid treatment, Carbon. 31 (1993) 109–121. doi:10.1016/0008-6223(93)90163-5.

[39] J.L. Figueiredo, M.F.R. Pereira, M.M.A. Freitas, J.J.M. Órfão, Modification of the surface chemistry of activated carbons, Carbon. 37 (1999) 1379–1389.

doi:10.1016/S0008-6223(98)00333-9.

[40] M.C. Román-Martínez, D. Cazorla-Amorós, A. Linares-Solano, C. Salinas-Martínez De Lecea, F. Atamny, Structural study of a phenolformaldehyde char, Carbon. 34 (1996) 719–727. doi:10.1016/0008-6223(95)00194-8.

[41] R. Zhong, Y. Qin, D. Niu, J. Tian, X. Zhang, X.-G. Zhou, S.-G. Sun, W.-K. Yuan, Effect of carbon nanofiber surface functional groups on oxygen reduction in alkaline solution, J. Power Sources. 225 (2013) 192–199. doi:10.1016/j.jpowsour.2012.10.043.

[42] G. Panomsuwan, S. Chiba, Y. Kaneko, N. Saito, T. Ishizaki, In situ solution plasma synthesis of nitrogen-doped carbon nanoparticles as metal-free electrocatalysts for the oxygen reduction reaction, J. Mater. Chem. A. 2 (2014) 18677–18686. doi:10.1039/c4ta03010a.

[43] P. Delhaes, M. Couzi, M. Trinquecoste, J. Dentzer, H. Hamidou, C. Vix-Guterl, A comparison between Raman spectroscopy and surface characterizations of multiwall carbon nanotubes, Carbon. 44 (2006) 3005–3013. doi:10.1016/j.carbon.2006.05.021.

[44] C. Vix-Guterl, J. Dentzer, P. Ehrburger, K. Méténier, S. Bonnamy, F. Béguin, Surface properties and microtexture of catalytic multi-walled carbon nanotubes, Carbon. 39 (2001) 318–320. doi:10.1016/S0008-6223(00)00247-5.

[45] D.W. Mckee, C.L. Spiro, K.E. J, P.G. Lamby, Catalytic Effects of Alkali Metal Salts in the Gasification of Coal Char, Symp. Coal Gasif. (1982) 74–86.

[46] K.H. van Heek, H.-J. Mühlen, Chemical Kinetics of Carbon and Char Gasification, in: J. Lahaye, P. Ehrburger (Eds.), Fundam. Issues Control Carbon Gasif. React., Springer Netherlands, Dordrecht, 1991: pp. 1–34. doi:10.1007/978-94-011-3310-4_1.

[47] B. McEnaney, Active Sites in Relation to Gasification of Coal Chars, in: J. Lahaye, P. Ehrburger (Eds.), Fundam. Issues Control Carbon Gasif. React., Springer Netherlands, Dordrecht, 1991: pp. 175–203. doi:10.1007/978-94-011-3310-4_10.

[48] A.B. Silva-Tapia, X. García-Carmona, L.R. Radovic, Similarities and differences in O2 chemisorption on graphene nanoribbon vs. carbon nanotube, Carbon. 50 (2012) 1152–1162. doi:10.1016/j.carbon.2011.10.028.

[49] T.W. Ebbesen, P.M. Ajayan, H. Hiura, K. Tanigaki, Purification of nanotubes, Nature. 367 (1994) 519–519. doi:10.1038/367519a0.

[50] N. Yao, V. Lordi, S.X.C. Ma, E. Dujardin, A. Krishnan, M.M.J. Treacy, T.W. Ebbesen, Structure and oxidation patterns of carbon nanotubes, J. Mater. Res. 13 (1998) 2432–2437. doi:10.1557/JMR.1998.0338.

[51] K. Morishita, T. Takarada, Scanning electron microscope observation of the purification

behaviour of carbon nanotubes, J. Mater. Sci. 34 (1999) 1169–1174. doi:10.1023/A:1004544503055.

[52] T. Shimada, H. Yanase, K. Morishita, J.I. Hayashi, T. Chiba, Points of onset of gasification in a multi-walled carbon nanotube having an imperfect structure, Carbon. 42 (2004) 1635–1639. doi:10.1016/j.carbon.2004.02.019.

[53] C. González-Gaitán, R. Ruiz-Rosas, E. Morallón, D. Cazorla-Amorós, Functionalization of carbon nanotubes using aminobenzene acids and electrochemical methods. Electroactivity for the oxygen reduction reaction, Int. J. Hydrogen Energy. 40 (2015) 11242–11253. doi:10.1016/j.ijhydene.2015.02.070.

[54] A. Gabe, R. Ruiz-rosas, C. González-gaitán, E. Morallón, D. Cazorla-amorós, Modeling of oxygen reduction reaction in porous carbon materials in alkaline medium . E ff ect of microporosity, (2018).

[55] A.J. Bard, L.R. Faulkner, Electrochemical Methods: Fundamentals and Applications, 2a., Wiley, 2001.

[56] M. Gara, R.G. Compton, Activity of carbon electrodes towards oxygen reduction in acid: A comparative study, New J. Chem. 35 (2011) 2647. doi:10.1039/c1nj20612e.

[57] P. Zhang, X. Hou, J. Mi, Y. He, L. Lin, Q. Jiang, M. Dong, From two-dimension to one-

dimension: the curvature effect of silicon-doped graphene and carbon nanotubes for oxygen reduction reaction, Phys. Chem. Chem. Phys. 16 (2014) 17479–17486. doi:10.1039/C4CP02167C.

[58] G.-L. Chai, Z. Hou, D.-J. Shu, T. Ikeda, K. Terakura, Active Sites and Mechanisms for Oxygen Reduction Reaction on Nitrogen-Doped Carbon Alloy Catalysts: Stone–Wales Defect and Curvature Effect, J. Am. Chem. Soc. 136 (2014) 13629–13640. doi:10.1021/ja502646c.

[59] K. Matsubara, K. Waki, Oxygen reduction characteristics of bamboo-shaped, multi-walled carbon nanotubes without nitrogen in acid media, Electrochim. Acta. 55 (2010) 9166–9173. doi:10.1016/j.electacta.2010.08.040.

[60] X. Pan, X. Bao, The effects of confinement inside carbon nanotubes on catalysis, Acc. Chem. Res. 44 (2011) 553–562. doi:10.1021/ar100160t.